REPORT DOCUMENTATION PAGE	Form Approved OMB No. 0704-0188

1. REPORT DATE (DD-MM-YYYY)	2. REPORT TYPE	3. DATES COVERED (From - To)
07122010	Journal Article	

4. TITLE AND SUBTITLE

First-order description of the mechanical fracture behavior of fine-grained surficial marine sediments during gas bubble growth

5a. CONTRACT NUMBER

5b. GRANT NUMBER
N00014-05-1-175

5c. PROGRAM ELEMENT NUMBER
0601153N

6. AUTHOR(S)

M.A. Barry, B.P. Boudreau, B.D. Johnson, and A.H. Reed

5d. PROJECT NUMBER

5e. TASK NUMBER

5f. WORK UNIT NUMBER
74-9867-09

7. PERFORMING ORGANIZATION NAME(S) AND ADDRESS(ES)

Naval Research Laboratory
Marine Geoacoustics Division
Stennis Space Center, MS 39529

8. PERFORMING ORGANIZATION REPORT NUMBER
NRL/JA/7430-09-3

9. SPONSORING/MONITORING AGENCY NAME(S) AND ADDRESS(ES)

Office of Naval Research
800 North Quincy Street
Arlington VA 22217-5000

10. SPONSOR/MONITOR'S ACRONYM(S)
ONR

11. SPONSOR/MONITOR'S REPORT

12. DISTRIBUTION/AVAILABILITY STATEMENT
Approved for public release; distribution is unlimited

13. SUPPLEMENTARY NOTES

J. Geophys Res., Vol. 115, F04029, doi: 10.1029/2010JF001833, 2010

14. ABSTRACT

[1] Bubbles in sediments, imaged via Computed Tomography (CT) scanning, and in surrogate transparent material (gelatin), are well-described geometrically as eccentric oblate spheroids. While sediments are undoubtedly visco-elasto-plastic solids, only part of that complex behavior appears to influence significantly the formation and shape of gas bubbles. Specifically, the shape of these bubbles can be explained if the mechanical response of fine-grained sediment is approximated by Linear Elastic Fracture Mechanics (LEFM). To determine the adequacy of the LEFM *approximation* for gas bubble growth in fine-grained sediments, a number of gas bubbles were injected and grown in natural sediments, while monitoring the size and shape using an industrial CT scanner.

15. SUBJECT TERMS

Linear Elastic Fracture Mechanics; (LEFM)

16. SECURITY CLASSIFICATION OF:			17. LIMITATION OF ABSTRACT	18. NUMBER OF PAGES	19a. NAME OF RESPONSIBLE PERSON
a. REPORT	b. ABSTRACT	c. THIS PAGE			Allen Reed
Unclassified	Unclassified	Unclassified	UU	10	19b. TELEPHONE NUMBER (Include area code) 228-688-5473

First-order description of the mechanical fracture behavior of fine-grained surficial marine sediments during gas bubble growth

M. A. Barry,[1] B. P. Boudreau,[1] B. D. Johnson,[1] and A. H. Reed[2]

Received 28 July 2010; revised 1 September 2010; accepted 10 September 2010; published 7 December 2010.

[1] Bubbles in sediments, imaged via Computed Tomography (CT) scanning, and in surrogate transparent material (gelatin), are well-described geometrically as eccentric oblate spheroids. While sediments are undoubtedly visco-elasto-plastic solids, only part of that complex behavior appears to influence significantly the formation and shape of gas bubbles. Specifically, the shape of these bubbles can be explained if the mechanical response of fine-grained sediment is approximated by Linear Elastic Fracture Mechanics (LEFM). To determine the adequacy of the LEFM *approximation* for gas bubble growth in fine-grained sediments, a number of gas bubbles were injected and grown in natural sediments, while monitoring the size and shape using an industrial CT scanner. A comparison of measured inverse aspect ratios (IARs) of the injected bubbles with calculated IARs from pressure records provides support for the LEFM theory. Deviations from LEFM are observable in the data, but as bubbles grow larger they trend more closely toward the theory. The use of LEFM has been shown to describe gas bubble growth in shallow coastal sediments to first order.

Citation: Barry, M. A., B. P. Boudreau, B. D. Johnson, and A. H. Reed (2010), First-order description of the mechanical fracture behavior of fine-grained surficial marine sediments during gas bubble growth, *J. Geophys. Res.*, *115*, F04029, doi:10.1029/2010JF001833.

1. Introduction

[2] Free gas is common in marine sediments, and it engenders several environmental and engineering problems. Bubbles in sediment scatter acoustic energy [*Anderson and Hampton*, 1980; *Judd and Hovland*, 1992; *Lyons et al.*, 1996], they alter seabed stability and geotechnical properties [*Hovland*, 1989; *Sills and Wheeler*, 1992; *Hovland et al.*, 2002], and, through transport to the surface and release to the atmosphere, they can affect the Earth's climate by releasing greenhouse gases [*Judd*, 2004].

[3] Miniscule gas bubbles reside in pore spaces, causing minimal sediment matrix deformation, but as bubbles grow larger than the pores, the structure of the sediment can change significantly. A model for spherical bubbles larger than the pore spaces was developed by *Wheeler* [1986], but *Johnson et al.* [2002] and *Boudreau et al.* [2005] have shown that bubbles in sediment are largely eccentric oblate spheroids, revealing a different structure, stress state, and accordingly, a differing mechanical behavior from that implied by spherical bubbles.

[4] Knowledge of the shape of bubbles in sediments and the mechanics of their growth and rise is not esoteric, but central both to the understanding of the flux of methane from sediments and to correct acoustic imaging beneath the ocean floor. Specifically, most acoustic models assume spherical bubbles [e.g., *Anderson and Hampton*, 1980]; however, such an approach does not yield good resolution for gassy sediments. Additionally, *Gardiner et al.* [2003] and *Algar and Boudreau* [2009] have shown that oblate spheroidal bubbles in sediments can grow at least two to four times faster than spherical bubbles, thus making shape an important factor in rates of methane production and bubble growth. The size distribution of bubbles in gassy sediments has been analyzed previously [*Gardner*, 1988; *Abegg and Anderson*, 1997; *Anderson et al.*, 1998; *Wilkens and Richardson*, 1998], but little work has focused on the shapes of these bubbles, in spite of the stated importance of shape.

[5] While other investigations have noted nonspherical bubble shapes in core samples [*Lyons et al.*, 1996; *Abegg and Anderson*, 1997; *Anderson et al.*, 1998; *Wilkens and Richardson*, 1998; *Best et al.*, 2004], none have provided a quantitative and testable explanation for the formation of the elliptical lens shapes. *Johnson et al.* [2002] reasoned that the shape was dictated by the particular mechanics of sediments. While fine-grained sediments are, in general, visco-elasto-plastic solids, near-spherical bubbles would be expected if the viscous and/or the plastic behaviors dominated the response of sediments to the stresses created by

[1]Department of Oceanography, Dalhousie University, Halifax, Nova Scotia, Canada.
[2]Naval Research Laboratory, Stennis Space Center, Mississippi, USA.

0148-0227/10/2010JF001833

bubble growth. *Johnson et al.* [2002] and *Boudreau et al.* [2005] were able to explain the shapes observed in experiments and nature by assuming that the bubbles were the result of fracture of a solid that was primarily elastic, at least in response to the stresses and the time scale associated with bubble growth. Furthermore, they suggested that the elastic response of surficial sediments could be approximated by Linear Elastic Fracture Mechanics (LEFM); the latter is a mechanical model for failure in brittle, elastic solids. Commonly used for rock mechanics, LEFM has been shown to be approximately true for other soft solids, such as gelatin [i.e., *Takada*, 1990; *Menand and Tait*, 2001] and soils [i.e., *Lima and Grismer*, 1994; *Murdoch*, 1993, 2002; *Hallett and Newson*, 2001; *Wang et al.*, 2007].

[6] Without visual evidence of bubble shapes in sediment, it is difficult to determine the validity of elastic and fracture deformation, and hence, the validity of LEFM for bubble growth. First, we review the elements of LEFM theory, and second, we establish the validity of LEFM by showing that bubbles injected into sediments and gelatin obey this theory.

2. Theoretical Background

[7] As the name implies, LEFM is comprised of two mechanisms, elastic and fracture deformations, combined in an energy balance. As internal pressure is applied to the walls of a crack, elasticity governs the behavior of the solid up to a critical stress level (P_c), above which fracture occurs. During elastic deformation, energy is stored in the medium. The medium's ability to retain elastic energy and resist fracture is dependent on the critical energy release rate, also known as the critical fracture energy (G_{IC}), a material property. The critical fracture energy of an elastic material is the energy required to create new free surfaces through the breaking of particle-particle bonds. The critical fracture energy is related to a second material property, the critical fracture toughness, K_{IC}, through

$$K_{IC} = \sqrt{(G_{IC}E)/(1-\nu^2)}, \tag{1}$$

for plane strain conditions, where E is Young's modulus and ν is Poisson's ratio of the solid [*Broek*, 1982].

[8] Theory based on fracture toughness assumes failure at a constant stress level at the crack tip, a valid assumption for materials with high strength and low toughness in plane strain conditions [*Broek*, 1982]. For a growing bubble in sediment, an oblate spheroid in an infinite medium should be a reasonable geometric approximation [*Johnson et al.*, 2002; *Boudreau et al.*, 2005] for plane strain conditions, leading to the following equation for the stress (P_c) needed for fracture (for a penny-shaped crack),

$$P_C = (K_{IC}\sqrt{\pi})/(2\sqrt{a}), \tag{2}$$

where a is the half length of the crack (see Figure 1). Plastic behavior will occur at the crack tip preventing stresses from approaching infinity (as predicted by theory); however, LEFM can still accurately predict the stress field surrounding the crack provided the plastic zone is small in comparison to the crack size [*Broek*, 1982].

[9] A second assumption made in our analysis is that the two-phase medium behaves as a single phase, that is, no pore water flow over the time scale of bubble growth. Thirdly, provided the crack is many times larger than the average pore or grain size, the medium will behave homogeneously. As the average crack sizes we have seen in previous experiments are greater than 10 mm and the average grain size of samples is in the range of 0.01 to 0.1 mm, our third assumption is valid.

[10] While (2) is useful in determining the stress field around a crack, it does not give any information about the bubble shape. This information is supplied by the crack-opening displacement (COD) equation, whereby the crack half-width (b) is defined as [*Sneddon*, 1946],

$$b = (4P_e(1-\nu^2)a)/(\pi E) \tag{3}$$

where P_e is the excess pressure in the crack above the in situ stress. Note that fracture occurs when $P_e = P_c$.

[11] Additionally, *Johnson et al.* [2002] combined fracture (2) and elasticity (3) with the volume of an oblate spheroid,

$$V = {}^4/_3(\pi a^2 b), \tag{4}$$

yielding an equation relating critical internal bubble overpressure (P_c) to bubble volume (V_{bub}),

$$P_C = \frac{K_{IC}^{6/5}\pi^{4/5}}{(24EV_{bub})^{1/5}}. \tag{5}$$

Johnson et al. [2002] further used the COD equation for plane stress in deriving the equation above, and upon correcting for plane strain, (5) becomes

$$P_C = \frac{K_{IC}^{6/5}\pi^{3/5}(1-\nu^2)^{1/5}}{(12EV_{bub})^{1/5}}. \tag{6}$$

[12] *Johnson et al.* [2002] showed that bubble growth during injection experiments consisted of an elastic growth phase followed by a fracturing phase. In the elastic phase, pressure increases and during fracture, rapid pressure drops occurred. The two growth phases are illustrated schematically in Figure 1, where elastic growth results in an increase in the crack half-width (b), while an increase in crack half-length (a) occurs during fracture.

3. Methods

[13] In order to examine the applicability of LEFM to bubble growth in sediments, Computed Tomography (CT) scanning of bubbles injected into sediments that are smaller in size than those reported in *Boudreau et al.* [2005] is required. Bubbles that were grown and subsequently CT-scanned by *Boudreau et al.* [2005] and *Algar* [2009] ranged from 170 to 2700 mm^3, significantly larger than most bubbles found in X-ray radiographs of pressurized cores [e.g., *Lyons et al.*, 1996]. To overcome this problem, the injection apparatus used by *Boudreau et al.* [2005] and *Algar* [2009] has been modified to accommodate the requirements above. In addition, the method of injection used previously does not mimic nature, as it involves incremental pressure increases to drive bubble growth. A diffusive method to deliver gas to a growing bubble is preferable, and this is incorporated in the modifications to the injector.

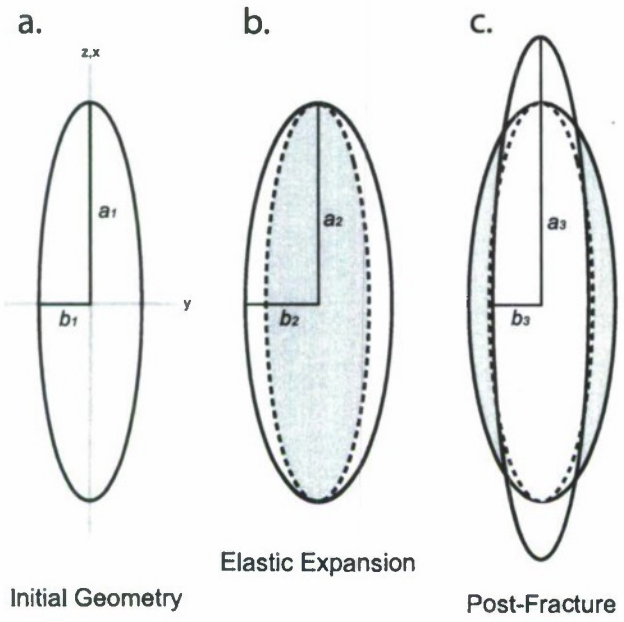

Figure 1. (a) Coordinates for an oblate spheroid with a and b defined as the half length and half width, respectively. (b) Elastic growth of an oblate spheroidal bubble predominantly in the short-axis (b) direction at pressure below that required for fracture (note that $a_2 = a_1$, but $b_2 > b_1$). (c) Fracture growth occurs along the long-axis (a) edge when bubble pressure reaches the critical pressure needed for fracture (note that $a_3 > a_2$).

3.1. Injection Apparatus

[14] The apparatus used for bubble injection (Figure 2) consists of a platform for the sediment core sample to rest on, with a movable stage below to allow insertion of a glass capillary upward into the sediment sample. The movable stage is on ball bearings and is raised and lowered using a geared motor to minimize disturbance of the sample. A small, stainless steel wire is located inside the capillary and is pushed into the sediment sample 2 mm above the top of the capillary to clear any blockage in the capillary and to create a small initial flaw in the sediment. The wire is sealed at the bottom using a small piece of rubber in a compression fitting (see Figure 2b).

[15] The apparatus has two pressure sensors on either side of a diffusive silicone membrane. On one side of the diffusive membrane (part 6 in Figure 2b) is the system dead volume (V_{sys}), which remains constant. The system dead volume is composed of the volume of parts 1–5 in Figure 2b. A second, adjustable volume (V_{adj}) is on the opposite side of the diffusive membrane and is composed of the volume of parts 7–9 in Figure 2b. The use of the diffusive membrane to grow bubbles by injection allows for small changes in system pressure, while also allowing for accurate calculation of gas bubble volume (V_{bub}). If we assume a constant PV of the entire system ($V_{adj} + V_{sys} + V_{bub}$), then V_{bub} can be calculated from the mole balance.

[16] Injection of air into the sample is achieved by elevating the system dead volume pressure via addition of gas through the silicone membrane. By decreasing V_{adj} with the use of a syringe, the pressure P_{adj} increases (constant PV), creating a pressure gradient across the membrane. Gas then diffuses through the membrane into V_{sys} at a rate proportional to the pressure drop across the membrane, thereby increasing P_{sys}. The diffusion of gas across the membrane is sufficiently slow to allow for small, controlled changes in P_{sys}. By monitoring the pressure inside the system, it is known when a bubble is formed (noticeable pressure drop). Using the pressure measured on both sides of the membrane, along with the changes in V_{adj}, bubble volume can be calculated.

[17] In order to monitor bubble pressure and volume during CT-scanning, the injection apparatus needs to be mounted onto the CT scanner platform with continuous monitoring of the bubble pressure outside of the CT scanner room. To achieve this, an injector base with a slip ring for all electrical connections was implemented to allow the injector and sample to be rotated through 360° during CT-scanning, while keeping electrical contact with the computer and power supply (part 15 of Figure 2b). Continuous pressure measurement during scanning allowed for P_e and V_{bub} to be monitored at all times during the CT scan.

3.2. Sediment Collection

[18] Thirty centimeter long sediment cores were collected from Canard, Nova Scotia, within the Minas Basin (Figure 3) for bubble injection and subsequent CT-scanning. Each core liner was composed of two 15 cm long halves of a liner, which were taped together to make one continuous liner. Core liners with a tapered bottom edge were pushed by hand into the sediment and removal was facilitated by digging around the liner to the depth of penetration.

[19] Cores were capped on both ends and sealed, while maintaining ~1 cm of seawater at the sediment surface. Cores were kept at 4°C until 24 hours prior to a bubble injection experiment, at which time the sample was placed in the CT-imaging room to acclimatize to room temperature (18°C). The sediment at the Canard site, where cores were collected, was fine sandy silt, with some clay-sized particles. Organic content averaged 4–5% and the sediment was functionally cohesive.

3.3. Gelatin Samples

[20] Due to the opaque nature of sediment and the cost of CT-scanning, a transparent alternative was desirable. Gelatin has been shown to behave in a brittle, elastic manner over a wide range of strains [*Takada*, 1990], so it was chosen as an analog medium for sediment [*Johnson et al.*, 2002]. As well, a wide range of strengths was easily achieved through changing the gelatin concentration and/or temperature. The range of strengths enabled determination of any changes in bubble growth behavior due to changing properties of the surrounding medium. Gelatin concentrations of 1.5–11.6% w/w (gelatin weight/water weight) were used at either 4°C or 20°C. Gelatin samples were prepared in both 0.1 × 0.1 × 0.1 m and 0.2 × 0.2 × 0.4 m (high) acrylic containers. Holes were predrilled in the container bottoms, through which the capillary of the injection device could penetrate. Bubble shapes were then measured using a camera and a calibrated grid. For sediment and gelatin samples, Young's modulus was measured using a simple uniaxial

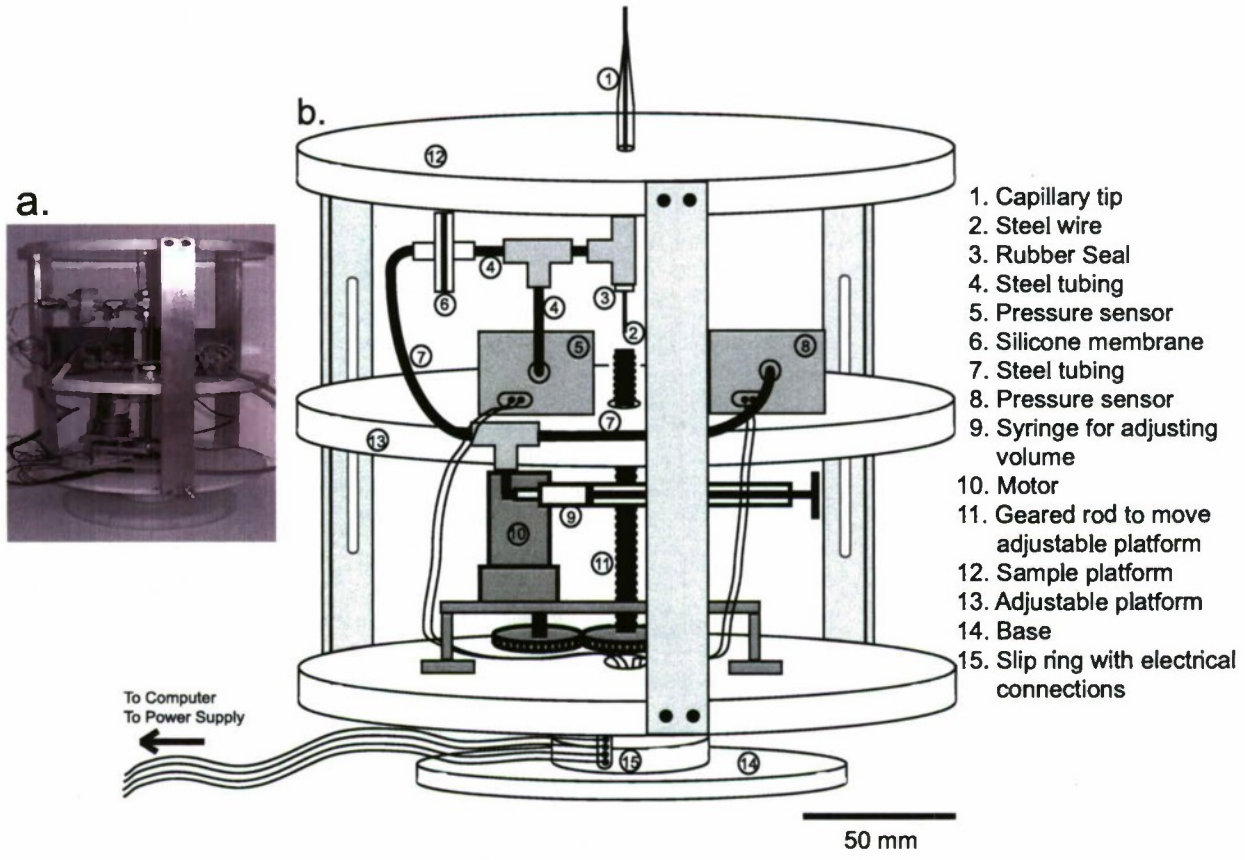

Figure 2. (a) Bubble injection apparatus. (b) Representative drawing of the injector detailing the mechanical parts. The setup allows for the injector tip to be mechanically inserted into the sample as well as allowing the samples to be turned during CT-scanning while remaining in electrical connection with the computer and power supply.

loading cell [*Johnson et al.*, 2002]. The elastic behavior during both loading and unloading was measured using a micrometer to an accuracy of 2.5×10^{-2} mm. Data showed a linear stress-strain response and were fitted to yield a value for Young's modulus.

3.4. CT Imaging

[21] Before bubble injection experiments with the modified injector, each sediment core was X-rayed to ensure samples contained no shells, burrows, or other major heterogeneities. Suitable cores were then cut in half using a thin wire, yielding two surfaces at 15 cm depth. Freshly cut surfaces were sealed with plastic wrap and placed on the injector stage, plastic down. The capillary was then inserted upward into the sample through the plastic seal. Once a bubble was formed, it was scanned using a high-resolution (to ≤ 10 μm) HD-500 CT scanner at the Naval Research Laboratory, NASA Stennis Space Center, Mississippi. When the three-dimensional (3D) scan was complete, additional gas was added to grow the bubble slightly, and subsequent scans were made after each growth period.

[22] The industrial CT scanner provided 1024×1024 pixel cross-section images, having pixel resolutions of 0.037 mm^2 (one bubble) and 0.046 mm^2 (two bubbles). The vertical distances between slices were 0.068 mm and 0.083 mm, respectively, and the resulting voxel (3D pixel) sizes of the CT scans were 1.76×10^{-4} mm^3 and 9.3×10^{-3} mm^3, respectively. The lateral two-dimensional (2D) slices of each bubble scan were then combined using the commercial 3D visualization software package Amira®.

4. Results

4.1. Bubble Injection

[23] Bubble injection into gelatin samples of various strengths produced bubbles that were oblate spheroids (Figure 4), displaying a circular face view (Figure 4a) and an elliptical side view (Figure 4b). The range of bubble sizes grown was 5–3000 mm^3, and the inverse aspect ratios (i.e., short axis/long axis, b/a) of the bubbles varied between 0.6 and 0.07, with the weakest gelatin resulting in the largest inverse aspect ratios (i.e., a shape closer to spherical).

[24] CT scans of bubbles grown by injection in sediment from the Minas Basin appear as thin crack-like features (Figure 5) with well-defined bubble walls. Three-dimensional reconstructions of bubbles grown via the injection method were made for numerous scans after injection-induced growth periods. Figures 6a–6c show three different bubbles grown by injection with bubble volume increasing from top to bottom in Figure 6. The oblate spheroidal geometry

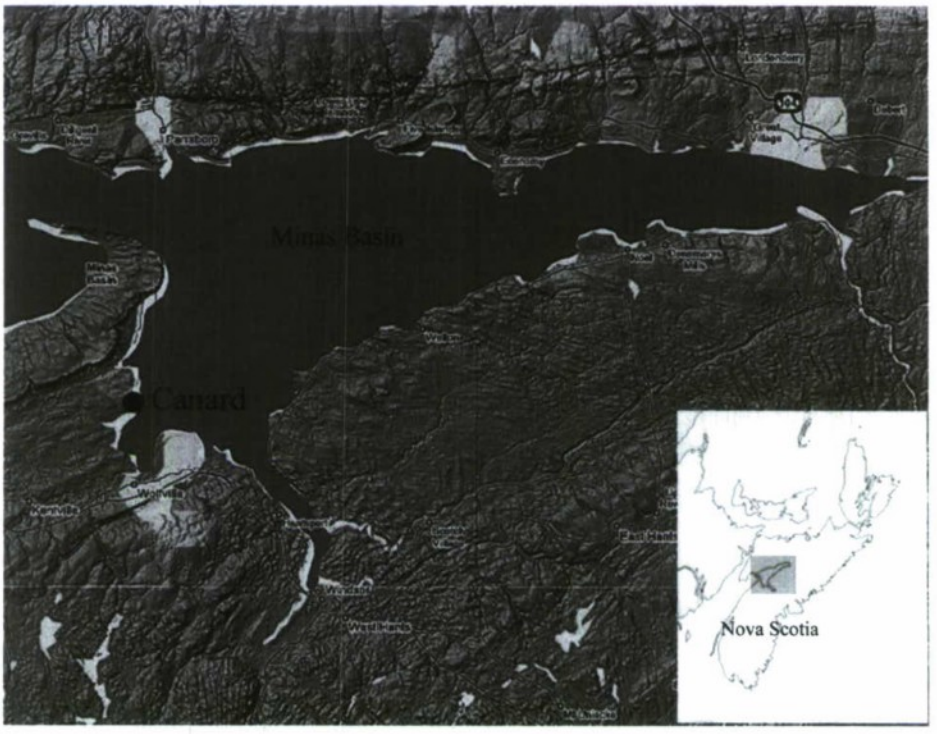

Figure 3. Map of field site, Canard, Nova Scotia, Canada.

appears to approximate the shapes of two bubbles (Figures 6a and 6b), and the initial volumes of the bubbles are nearly an order of magnitude smaller than previous CT-seanned bubbles grown via the injection method [see *Boudreau et al.*, 2005; *Algar*, 2009]. In Figure 6c the bubble initially grows upward, perpendicular to the smallest stress direction, but deviates to a horizontal growing plane.

[25] Given that the bubbles can be approximated as oblate spheroids, theoretical aspect ratios can be determined from the pressure and volume records and compared to the actual measured shapes to determine the validity of LEFM for the description of gas bubble growth in sediment, as well as in other soft solids, such as gelatin.

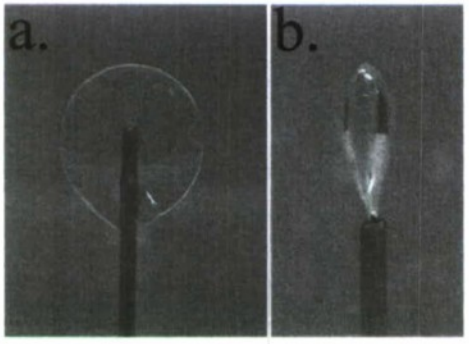

Figure 4. Injected bubbles in gelatin: (a) Face view; (b) side view. The capillary is 1.5 mm wide. The shape is very closely approximated by an oblate spheroid.

4.2. LEFM Validation

[26] A bubble's inverse aspect ratio (IAR) is valuable in determining the validity of the assumption of elastic behavior for sediment and other soft solids during bubble growth by fracture. Rearranging (3) yields an expression for crack

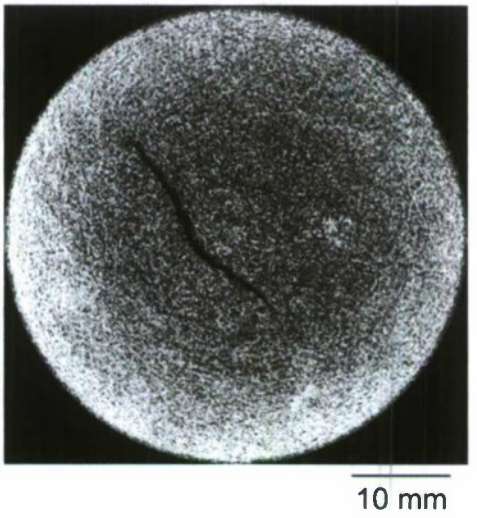

Figure 5. Cross-sectional CT image slice of a bubble grown in sediment. Bubble volume is 120 mm^3, maximum width is 23 mm, thickness is 0.7 mm, and length is 21 mm. Reconstructed 3D image of the bubble can be seen in Figure 6b.

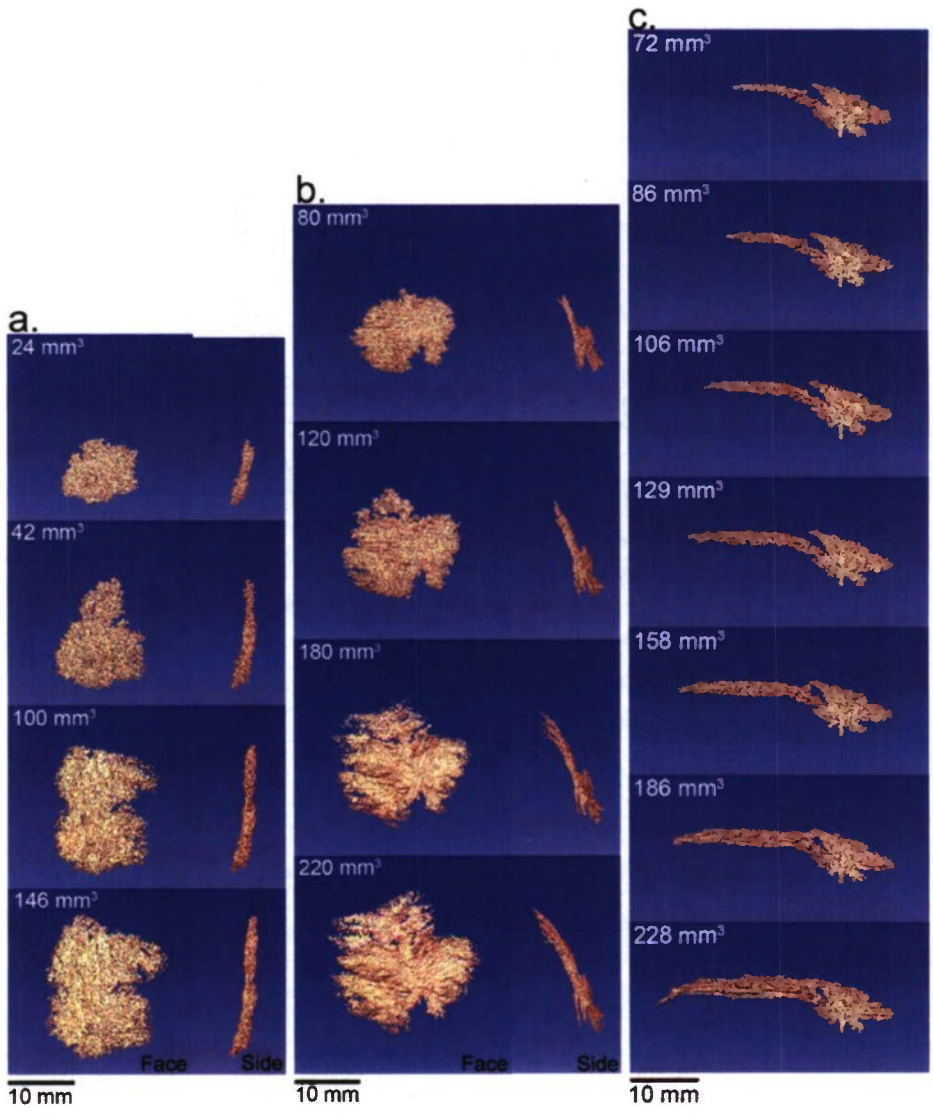

Figure 6. Reconstructed 3D images of three bubbles grown via injection in sediment. In all three cases, the bubble grew upward and outward, but not downward. (a–c) Three different bubbles grown in small volume increments and scanned after each growth period. The third bubble (Figure 6c) shows upward growth deviation, perhaps due to a stronger layer or a plane of weakness, upon which the bubble deflects its growth to become horizontal.

(bubble) IAR that is linearly related to bubble overpressure (P_e):

$$IAR = (4P_e(1-\nu^2))/(\pi E), \quad (7)$$

where overpressure is the measured internal pressure minus the atmospheric and overburden pressures. Equation (7) relates two dimensionless quantities, the IAR on the left-hand side and an unnamed grouping of P_e (K_{IC}), ν, and E on the right-hand side. This then defines a similarity relationship for bubbles that grow and/or form in solids via LEFM.

[27] A plot of calculated IARs from (7) versus measured IARs from gelatin and sediment should yield a straight line with a slope of unity, if both behave elastically during bubble growth. In Figure 7 the IARs calculated from pressure records are plotted against the measured IARs from CT scans (sediment) and camera images (gelatin). Injected gas bubbles in both gelatin and sediment fall near the 1:1 line, providing evidence to the first-order for the use of LEFM to describe bubble growth in soft elastic solids.

[28] A second way of comparing the data is to look at how IARs change as bubble volume increases. LEFM predicts that as a bubble grows in length (a), the pressure will decrease (2), and this will result in a decrease in IAR (3). Records in gelatin show a decrease in pressure as a bubble grows by fracture and, as a result, the calculated IAR also decreases. Measured IARs also decrease in gelatin, as bubbles grow larger in volume, becoming more and more eeeentrie (Figure 8).

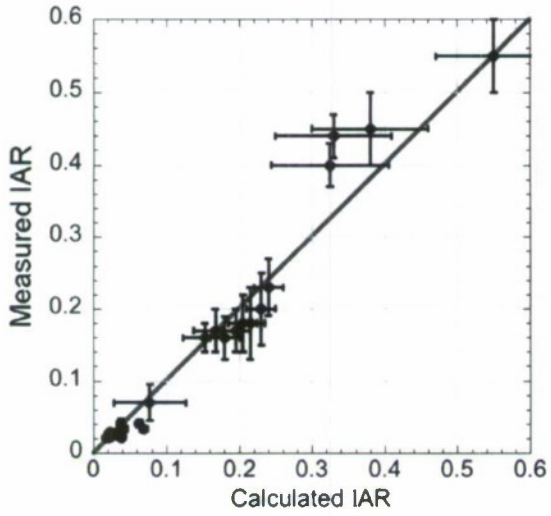

Figure 7. Plot of the measured inverse aspect ratios (IARs) and the calculated theoretical IARs for all gelatin and sediment samples. Errors in calculated IARs are based on the range of measured values of Young's modulus in each sample (i.e., maximum and minimum values of E), while errors in measured IARs are taken to be 25%, due to human error in estimation; predominantly of bubble width, but also of bubble length and precision of the CT scanner (sediment only).

[29] As the objective is to determine the applicability of LEFM to bubble growth in sediments, the patterns seen in gelatin, which is a linear-elastic material, should be replicated in sediment experiments. All of the bubble IARs in sediment plot in the far bottom left corner of Figure 7, and to more usefully illustrate these bubbles, data for the first two bubbles in Figure 6 are shown in Figure 9. The bubble shapes are well-characterized by LEFM, with most data plotting very near or on the 1:1 measured to calculated IAR line. Also, as with gelatin bubbles, the IARs of the bubbles grown in sediment decrease with increasing volumes. The bubble grown by *Boudreau et al.* [2005] is also plotted and it falls very near the 1:1 line as well. The *Boudreau et al.* [2005] bubble is significantly larger (Figure 9b), but its IAR is larger due to differing sediment mechanical properties.

5. Discussion

[30] From CT scans of three injected gas bubbles in sediments, it can be seen that two of the bubbles (Figures 6a and 6b) are closely approximated by thin, circular cracks, while the third bubble (Figure 6c) can only be approximated as a thin crack. Not only can the shape be seen to approximate a crack, but additionally, LEFM can be used to estimate both the size and IAR of bubbles grown in gelatin and in uniform sediment. LEFM theory for bubble growth in sediments can be extended from bubble sizes of 170–2700 mm^3 [*Boudreau et al.*, 2005; *Algar*, 2009], to volumes as small as 24 mm^3, which gives a diameter of approximately 3.6 mm (spherical equivalent). This is still more than an order of magnitude above the grain scale. Looking at the 3D images in Figures 6a and 6b, one can see the bubble geometries are approximated by thin penny-shaped cracks at the length scale of the bubble, while the majority of the variability in shape is at much smaller spatial scales. The bubbles grown in this study are of the same order of volume as natural bubble sizes reported by others [*Lyons et al.*, 1996; *Abegg and Anderson*, 1997; *Anderson et al.*, 1998].

[31] The validity of elastic COD theory for describing bubble shape is seen in the theoretical (calculated) versus measured IAR plot (Figure 7). The measured IARs in gelatin and sediment are approximately the same as the calculated IARs from the bubble pressure and the mechanical properties, within measurement errors. In sediment, the measured IARs of bubbles are well-described by LEFM, despite the heterogeneities that natural sediment samples are likely to possess.

[32] As bubble size becomes smaller, inverse aspect ratios continue to increase, that is, the smallest bubble grown in gelatin had an IAR greater than 0.5. Thus, it is expected that as bubble size is further reduced the IAR will continue to increase until the bubble becomes spherical (IAR = 1) at pore size volumes. The result of an increased IAR is a decrease in the stress concentration at the ends of the long axes of the bubble to a finite value. Looking at the two dimensional case of an ellipse in a plate, the stress concentration (σ) at the edge of the long axis (a) is defined as [*Pilkey et al.*, 2008]

$$\sigma = P\left(1 + 2\frac{a}{b}\right), \tag{8}$$

where b is the short axis length of the oblate spheroid (Figure 1).

[33] As the IAR decreases, the finite stress at the edges of the crack becomes larger, and at an IAR of approximately

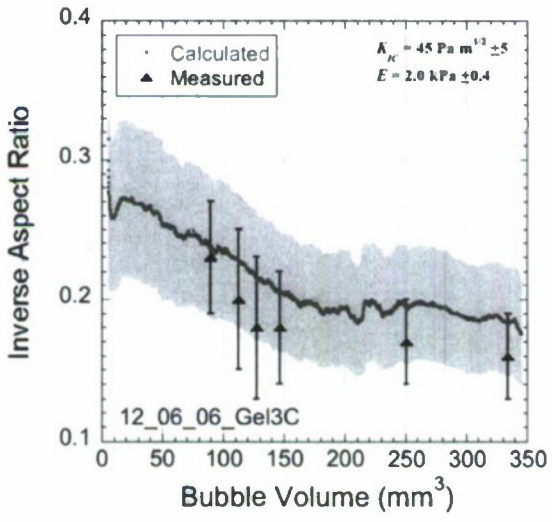

Figure 8. Plot of inverse aspect ratio (IAR) versus bubble volume in a gelatin sample. The error in IAR (calculated, shaded area; measured, black lines) is the same as in Figure 7. Error in bubble volume is not plotted, but is estimated at 5% due to uncertainty in the adjustable and system volumes. As the bubble grows, the IAR decreases.

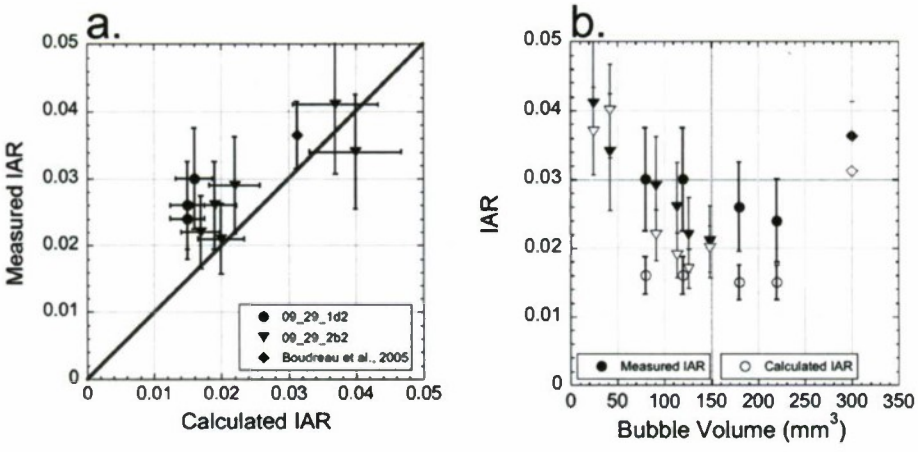

Figure 9. (a) Measured versus calculated IARs for bubbles grown in sediment. Bubbles from Figures 6a and 6b are plotted along with the bubble grown by *Boudreau et al.* [2005]. To a first approximation, the data fall near or on the 1:1 line for bubbles that approximate an oblate spheroid. (b) As bubble volume increases the IAR decreases, as expected from linear elastic fracture mechanics theory. The bubble from *Boudreau et al.* [2005] was grown in sediment with differing properties and so it does plot on the same trend of decreasing IAR with volume as the two bubbles grown in this study. Error in IAR is the same as in Figure 7.

0.1 and smaller, the localized stress concentration becomes large enough that LEFM predicts the stress field accurately, with the exception of the area extremely close to the crack tip. However, bubbles in gelatin with large IARs appear to behave according to LEFM to a high degree of accuracy, predicting IARs up to values as great at 0.5. This may indicate that LEFM constitutes an appropriate model for sediment bubbles that are much smaller than those grown via injection, where it is expected that as bubble sizes decrease, IARs increase, provided the sediment can still be described by an elastic continuum (i.e., the bubbles are larger than the pores).

[34] Nonspherical gas bubbles are of geotechnical concern because they change the behavior of sediment when loaded. While spherical bubbles do create stress concentrations, these increases in local stress are amplified along the edge of oblate spheroidal bubbles. Take the 2D example of a circular hole in a plate (Figure 10). Loading the plate along the top surface results in a localized stress in the horizontal plane that bisects the circular hole that is three times greater than the applied stress at the edge of the plate. Replacing the circular hole with a horizontally lying ellipse with an aspect ratio of 1:10, the stress along the horizontal plane that bisects the ellipse is amplified to 21 times the applied stress, a sevenfold increase over a circular hole.

[35] *Wheeler* [1986] and *van Kessel and van Kesteren* [2002] considered how gas bubbles might rise through sediment and reach the sediment-water interface, both concluding that spherical bubbles are not likely to rise in sediments and that spherical bubbles would need to be approximately 1 m in diameter to rise due to buoyancy and plastic yielding of sediment. *Martens and Klump* [1980] have shown centimeter-scale bubble release from sediments at Cape Lookout Bight, on a tidal cycle, begging the question of how both the gas bubbles and the sediments behave for gas to be released.

[36] *van Kessel and van Kesteren* [2002] suggest that bubbles could grow into previously formed cracks. CT images of the injected bubbles grown in this study show that fractures may be formed due to bubble growth alone, but bubbles will also likely exploit planes of weakness or pre-existing cracks if available (e.g., Figure 6c). Given that plastic yielding of sediment in response to bubble rise in sediment does not reflect the observed time scales seen in nature, elastic fracture may explain the rise of much smaller gas bubbles. Bubbles growing by fracture may exploit the pressure gradient to fracture preferentially toward the surface, as is seen in the bubble injection experiments in both sediment and gelatin. Once a bubble reaches a critical size, growth upward will be balanced by crack closure at the bottom, maintaining a nearly constant bubble volume. This has been shown to occur in bubble rise experiments in gelatin [e.g., *Takada*, 1990; *Bons et al.*, 2001; *Rivalta et al.*, 2005].

[37] The results presented also provide support for the LEFM bubble growth mechanisms used by *Gardiner et al.* [2003] and *Algar and Boudreau* [2009], both of which lead to more rapid bubble growth in organic-rich sediments. While spherical, viscous-plastic models of bubble growth predict typical bubble sizes to be formed over periods of weeks to months, a diffusion-LEFM-coupled model predicts the same size bubbles in days. *Gardiner et al.* [2003] and *Algar and Boudreau* [2010] have also shown that under LEFM behavior, bubble growth may become arrested under weak methane source strength conditions.

[38] It is anticipated that the sediment will have small-scale heterogeneities that will cause small changes in both fracture toughness and Young's modulus, both of which will affect bubble shape and pressure. As a result any attempt to do a detailed comparison of predicted and measured aspect ratios will be hindered in natural sediments. In the case of the bubble in Figure 6c, the shape is drastically different

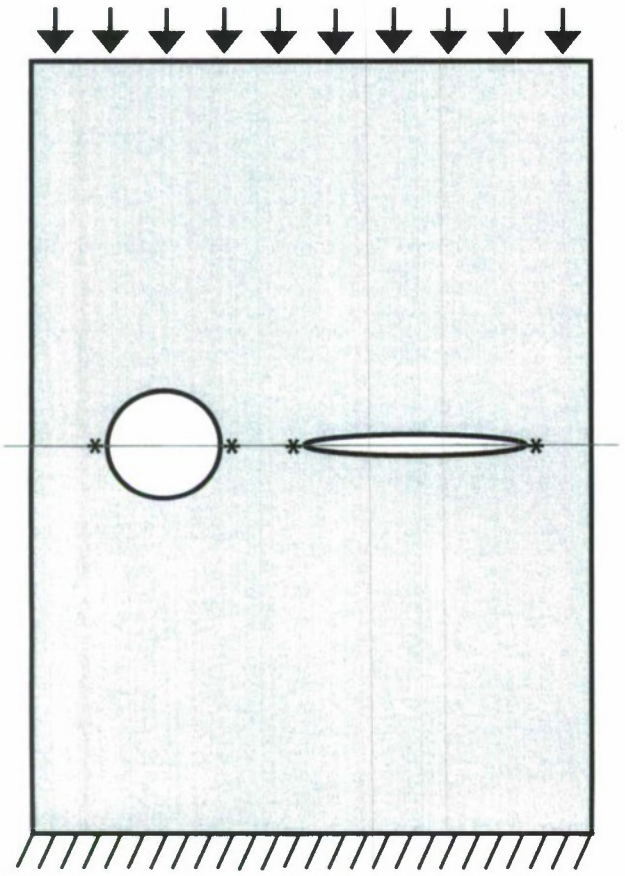

Figure 10. A plate fixed at its base and loaded with pressure (P) at the top and containing a circular and an ellipse void. Pressure on the voids results in localized stress concentrations at the edges of the voids and perpendicular to the stress applied (denoted by asterisks).

from an oblate spheroid, precluding a comparison of measured and calculated IARs.

6. Conclusions

[39] CT-scanning of gas bubbles in fine-grained sediments has shown that they are eccentric oblate spheroids, to a first approximation. The shapes and the inverse aspect ratios of these bubbles are further consistent with the predictions made by LEFM. Bubbles in sediments do exhibit secondary deviations from the predictions of LEFM; however, they are not large and can be explained by small heterogeneities at smaller scales. These results do not preclude the visco-elasto-plastic behavior of sediment for all geomechanical problems, but in the case of growing gas bubbles, LEFM is shown to be a good predictor of bubble shape.

Notation

a Crack half length mm
b Crack half width mm
E Young's modulus kPa
G_{IC} Critical fracture energy N m^{-1}
K_{IC} Critical fracture toughness Pa m$^{1/2}$
P Pressure kPa
P_c Critical stress level kPa
P_e Excess pressure kPa
P_{adj} Adjustable volume pressure kPa
P_{sys} System volume pressure kPa
V Volume mm^3
V_{bub} Bubble volume mm^3
V_{adj} Adjustable volume mm^3
V_{sys} System volume mm^3
ν Poisson's ratio –
σ Stress concentration kPa
IAR Inverse aspect ratio (b/a)
COD Crack-opening displacement
CT Computed tomography
LEFM Linear Elastic Fracture Mechanics

[40] **Acknowledgments.** We gratefully acknowledge support for this work by the US Office of Naval Research under Grants N00014-05-1-175 and N00014-08-1-0818 and a NSERC Discovery Grant to BPB. The CT-scanning work was also supported by NRL Base Funding, PE#0601153N. We thank the anonymous reviewers for their critical, but enlightening comments.

References

Abegg, F., and A. L. Anderson (1997), The acoustic turbid layer in muddy sediments of Eckernförde Bay, Western Baltic: Methane concentration, saturation, and bubble characteristics, *Mar. Geol.*, *137*, 137–147.

Algar, C. K. (2009), Bubble growth and rise in soft, fine-grained sediments, Ph.D. thesis, Dalhousie Univ., Halifax, Nova Scotia, Canada.

Algar, C. K. and B. P. Boudreau (2009), Transient growth of an isolated bubble in muddy, fine-grained sediments, *Geochim. Cosmochim. Acta*, *73*, 2581–2591, doi:10.1016/j.gca.2009.02.008.

Algar, C. K. and B. P. Boudreau (2010), Stability of bubbles in a linear elastic medium: Implications for bubble growth in marine sediments, *J. Geophys. Res.*, *115*, F03012, doi:10.1029/2009JF001312.

Anderson, A. L., and L. D. Hampton (1980), Acoustics of gas-bearing sediments, II: Measurements and models, *J. Acoust. Soc. Am.*, *67*, 1890–1903.

Anderson, A. L., F. Abegg, J. A. Hawkins, M. E. Duncan, and A. P. Lyons (1998), Bubble populations and acoustic interaction with the gassy floor of Eckernförde Bay, *Cont. Shelf Res.*, *18*, 1807–1838.

Best, A. I., M. D J. Tuffin, J. K. Dix, and J. M. Bull (2004), Tidal height and frequency dependence of acoustic velocity and attenuation in shallow gassy marine sediments, *J. Geophys. Res.*, *109*, B08101, doi:10.1029/2003JB002748.

Bons, P. D., J. Dougherty-Page, and M. A. Elburg (2001), Stepwise accumulation and ascent of magmas, *J. Metamorph. Geol.*, *19*, 625–631, doi:10.1046/j.0263-4929.2001.00334.x.

Boudreau, B. P., C. Algar, B. D. Johnson, I. Croudace, A. Reed, Y. Furukawa, K. M. Dorgan, P. A. Jumars, A. S. Grader, and B. S. Gardiner (2005), Bubble growth and rise in soft sediments, *Geology*, *33*, 517–520, doi:10.1130/G21259.1.

Broek, D. (1982), *Elementary Engineering Fracture Mechanics*, 3rd Ed., Kluwer Academic Publishers, Boston, Mass.

Gardiner, B. S., B. P. Boudreau, and B. D. Johnson (2003), Growth of disk-shaped bubbles in sediments, *Geochim. Cosmochim. Acta*, *67*, 1485–1494, doi:10.1016/S0016-7037(02)01072-4.

Gardner, T. N. (1988), The acoustic properties of gassy soil, Ph.D. thesis, Univ. of Oxford, Oxford, U.K.

Hallett, P. D. and T. A. Newson (2001), A simple fracture mechanics approach for assessing ductile crack growth in soil, *Soil Sci. Soc. Am. J.*, *65*, 1083–1088.

Hovland, M. (1989), The formation of pockmarks and their potential influence on offshore construction, *Q. J. Eng. Geol. Hydrogeol.*, *22*, 131–138.

Hovland, M., J. V. Gardner, and A. G. Judd (2002), The significance of pockmarks to understanding fluid flow processes and geohazards, *Geofluids*, *2*, 127–136, doi:10.1046/j.1468-8123.2002.00028.x.

Johnson, B. D., B. P. Boudreau, B. S. Gardiner, and R. Maass (2002), Mechanical response of sediments to bubble growth, *Mar. Geol.*, *187*, 347–363, doi:10.1016/S0025-3227(02)00383-3.

Judd, A. G. (2004), Natural seabed gas seeps as sources of atmospheric methane, *Environ. Geol.*, *46*, 988–996, doi:10.1007/s00254-004-1083-3.

Judd, A. G., and M. Hovland (1992), The evidence of shallow gas in marine sediments, *Cont. Shelf Res.*, *12*, 1081–1095.

Lima, L. A., and M. E. Grismer (1994), Application of fracture mechanics to cracking of saline soils, *Soil Sci.*, *158*, 86–96.

Lyons, A. P., M. E. Duncan, A. L. Anderson, and J. A. Hawkins (1996), Predictions of the acoustic scattering response of free-methane bubbles in muddy sediments, *Acoust. Soc. Am. J.*, *99*, 163–172.

Martens, C. S., and J. V. Klump (1980), Biogeochemical cycling in an organic-rich coastal marine basin, I: Methane sediment-water exchange processes, *Geochim. Cosmochim. Acta*, *44*, 471–490.

Menand, T. and S. R. Tait (2001), A phenomenological model for precursor volcanic eruptions, *Nature*, *411*, 678–680, doi:10.1038/35079552.

Murdoch, L. C. (1993), Hydraulic fracturing of soil during laboratory experiments: Parts 1–3, *Géotechnique*, *43*, 255–287.

Murdoch, L. C. (2002), Mechanical analysis of idealized shallow hydraulic fracture, *J. Geotech. Geoenviron. Eng.*, *128*, 488–495, doi:10.1061/(ASCE)1090-0241(2002)128:6(488).

Pilkey, W., D. Pilkey, and R. E. Peterson (2008), *Peterson's Stress Concentration Factors*, 3rd Ed., John Wiley and Sons, New Jersey.

Rivalta, E., M. Bottinger, and T. Dahm (2005), Buoyancy-driven fracture ascent: Experiments in layered gelatine, *J. Volcanol. Geotherm. Res.*, *144*, 273–285, doi:10.1016/j.jvolgeores.2004.11.030.

Sills, G. C. and S. J. Wheeler (1992), The significance of gas for offshore operations, *Cont. Shelf Res.*, *12*, 1239–1250, doi:10.1016/0278-4343(92)90083-V.

Sneddon, I. N. (1946), The distribution of stress in the neighborhood of a crack in an elastic solid, *Proc. Roy. Soc. London, Ser. A*, *187*, 229–260.

Takada, A. (1990), Experimental study on propagation of liquid-filled crack in gelatin: Shape and velocity in hydrostatic stress condition, *J. Geophys. Res.*, *95*(B6), 8471–8481, doi:10.1029/JB095iB06p08471.

van Kessel, T. and W. G. M. van Kesteren (2002), Gas production and transport in artificial sludge deposits, *Waste Manage.*, *22*, 19–28, doi:10.1016/S0956-053X(01)00021-6.

Wang, J.-J., J.-G. Zhu, C. F. Chiu, and H.-J. Chai (2007), Experimental study on fracture behavior of a silty clay, *Geotech. Test. J.*, *30*, 1–9, doi: 10.1520/GTJ100715.

Wheeler, S. J. (1986), Stress-strain behavior of soils containing gas bubbles, Ph.D. thesis, Univ. of Oxford, Oxford, U. K.

Wilkens, R. H. and M. D. Richardson (1998), The influence of gas bubbles on sediment acoustic properties: In situ, laboratory, and theoretical results from Eckernförde Bay, Baltic Sea, *Cont. Shelf Res.*, *18*, 1859–1892, doi:10.1016/S0278-4343(98)00061-2.

M. A. Barry, B. P. Boudreau, and B. D. Johnson, Department of Oceanography, Dalhousie University, 1355 Oxford St., Halifax, NS, B3H 4J1, Canada. (barrym@dal.ca)

A. H. Reed, Naval Research Laboratory, Code 7432, Stennis Space Center, MS 39529, USA.